

# Ion Tracing in Gas Dynamic Flow Fields: A Case Study on the Ion Funnel

Athanasios Zacharos<sup>2</sup>; Alexander Lekkas<sup>1</sup>; Michael Sudakov<sup>1</sup>; Dimitris Papanastasiou<sup>1</sup>; Diamantis Kounadis<sup>1</sup>; Ioannis Nikolos<sup>2</sup>; Emmanuel Raptakis<sup>1</sup>

<sup>1</sup>Fasmatech Science & Technology, Athens, GR; <sup>2</sup>Technical University of Crete, Chania, GR

## INTRODUCTION

High performance Atmospheric Pressure Ionization Mass Spectrometry (API MS) relies heavily on intermediate pressure ion optics design to enhance transmission efficiency. The ion funnel is one of the most recent technological advancements in the field with a significant impact on instrument sensitivity. Characterization of the ion funnel has been mainly accomplished experimentally and to some extent by ion optical simulations performed in a gas under equilibrium conditions. Here the Direct Simulation Monte Carlo (DSMC) method is applied to investigate under-expanded flows discharging into a “breathless” ion funnel structure. The investigation is extended to ion optics simulations incorporating the computed flow fields in order to investigate transmission characteristics and mass discrimination effects.

## INLET BOUNDARIES

The procedure to obtain accurate inlet boundary conditions for the DSMC calculations is rather elaborate and involves preliminary computations based on the Reynolds-Averaged Navier-Stokes (RANS) method for the high pressure region of the domain, which includes a 65 mm long 0.5 mm i.d. capillary inlet, the high pressure region (1 bar) upstream and the free jet expansion region downstream inside a low pressure vacuum chamber. Figures 1 (a) and (b) show the 3D flow domain constructed in CATIA and the mesh in ANSYS respectively. The high density mesh near the symmetry axis ensures precise computations at elevated pressure and accurate representation of the supersonic near-field region of the jet.

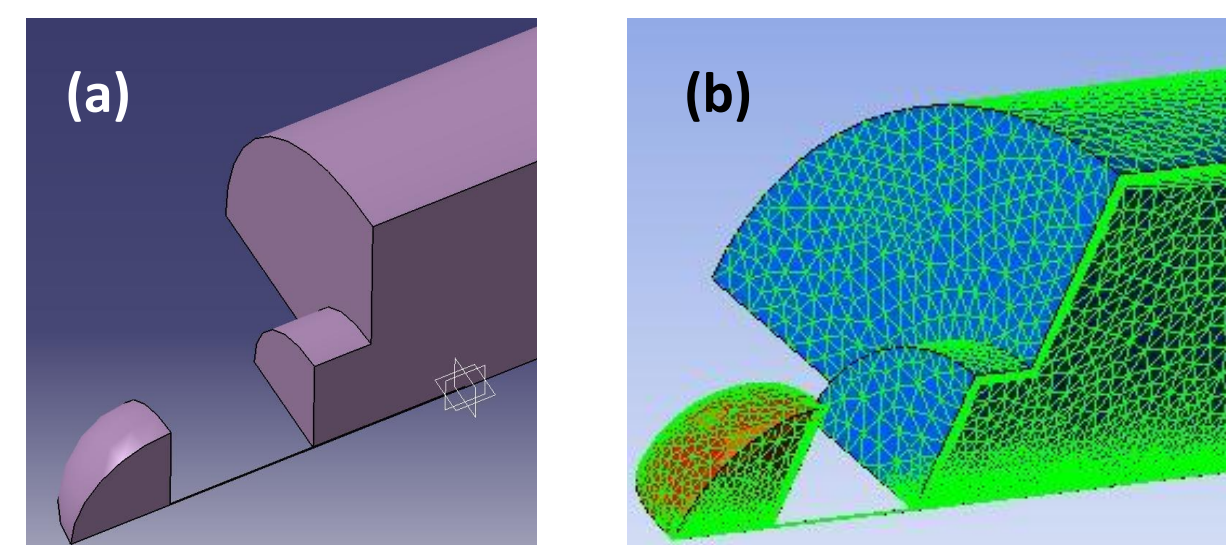


FIGURE 1. (a) Flow domain constructed in CATIA and (b) mesh generated in ANSYS.

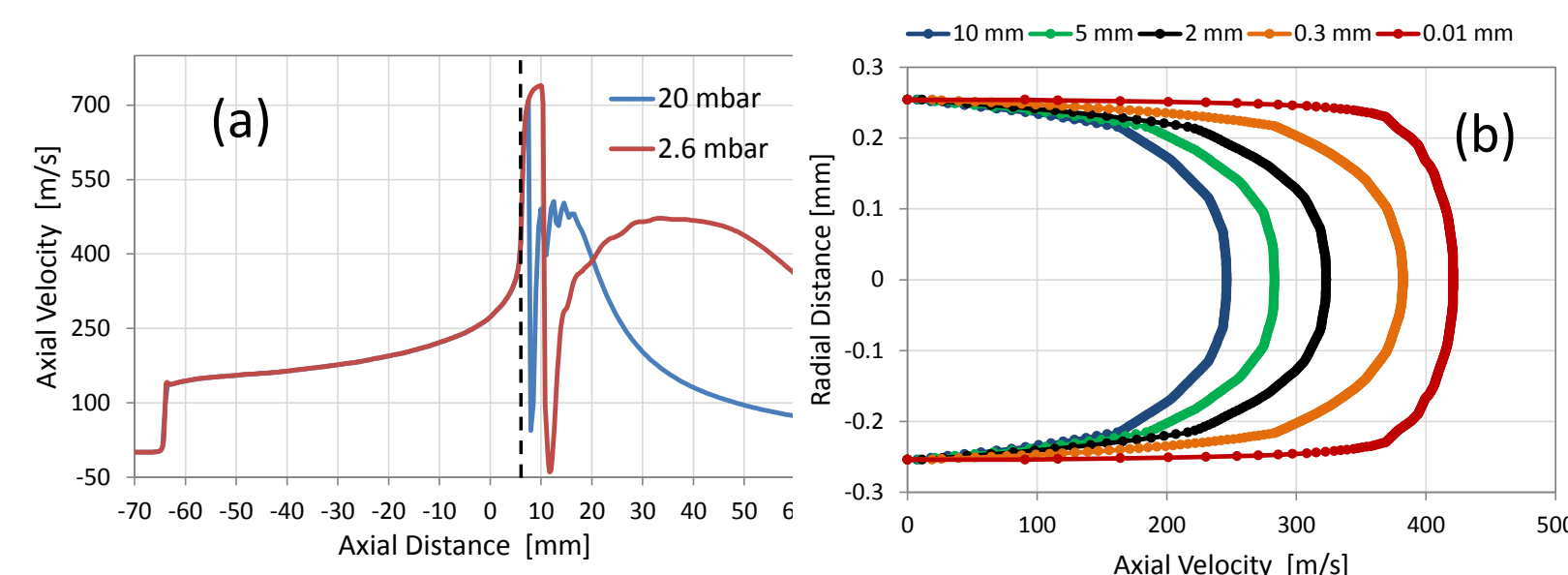


FIGURE 2. (a) Axial velocity profiles along the symmetry axis and (b) radial velocity profiles of the capillary flow. Distance values are relative to the exit of the capillary.

Figure 2 (a) shows the axial velocity along the symmetry axis extending from the high pressure region throughout the capillary and into the near-field region of the under-expanded flow. Radial velocity profiles inside the capillary are shown in Figure 2 (b). Distance values are relative to the capillary exit. The two cases examined (2.6 mbar & 20 mbar) indicate the choked character of the flow where velocity profiles are independent of the background pressure inside the vacuum chamber.

## DIRECT SIMULATION MONTE CARLO

Bird’s DS2V serial code is employed for the 2D axisymmetric DSMC calculations to solve the under-expanded jet and the flow field developed inside the ion funnel. The inlet boundary conditions were determined in two consecutive steps. The first step involves the application of the RANS equations as described above and the second step the application of the DSMC method across the last 2 mm of the capillary including the first few mm of the under-expanded flow. Progressive calculation of the flow field using different computational tools resolves basic problems associated with accuracy and convergence period as highlighted further below.

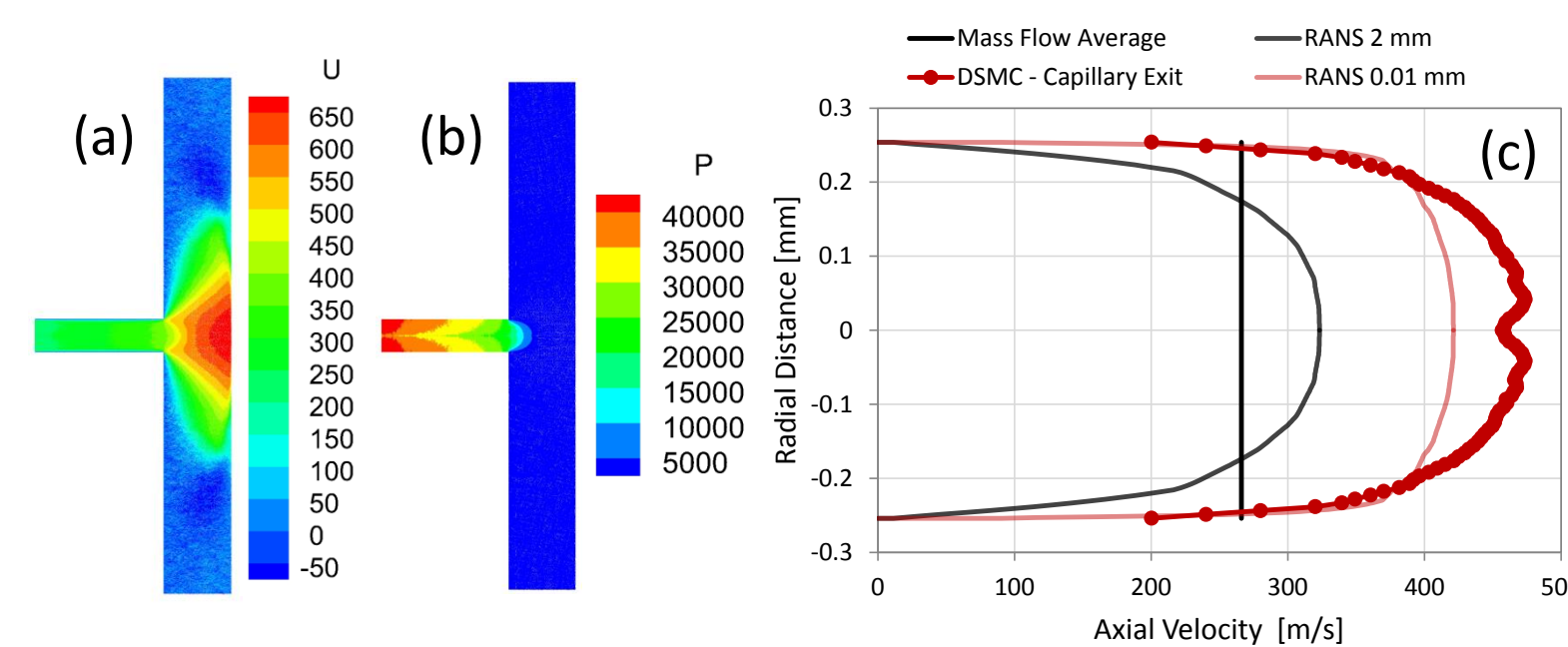


FIGURE 3. (a) Velocity and (b) pressure flow fields near the capillary exit obtained with the DSMC method. (c) RANS and DSMC radial velocity profiles inside the capillary.

Figures 3 (a) and (b) show velocity and pressure flow fields across the capillary exit and the onset of the supersonic flow. Figure 3 (c) shows radial velocity profiles obtained from the RANS equations and the DSMC method. The DSMC inlet boundary at 2 mm from the capillary exit is calculated from the RANS equations. A uniform velocity profile is imposed at the capillary inlet boundary of the DSMC model based on the mass-flow average of the RANS parabolic profile. The calculation is performed using the following expression:

$$\bar{V} = \frac{1}{\bar{\rho}} \int_0^r \rho 2\pi r^2 V(r) dr$$

where  $\bar{V}$  is the mass-flow average velocity,  $\rho$  is density and  $r$  is radial distance. Similar expressions were used for the determination of temperature and gas density. A “vacuum” boundary is imposed at the outlet of the short DSMC flow domain shown in Figures 3 (a) and (b) to ensure that supersonic flow conditions are established and no information travels backwards.

Figure 3 also compares the two radial velocity profiles at the capillary exit obtained with the RANS and DSMC methods respectively. The RANS solution shows no-slip conditions, in contrast to the DSMC profile demonstrating the formation of a slip velocity boundary of the order of  $\sim 200$  m/s. This discrepancy shows that an accurate solution of the free jet flow cannot be obtained with the RANS approach unless the slip velocity near the capillary exit is known. The properties of the DSMC flow at the capillary exit are then used for setting up the inlet boundaries of the ion funnel model in order to increase the minimum integration step determined by the highest pressure in the flow domain and therefore reduce computational time. For the flow field presented below the maximum pressure at the capillary exit is  $\sim 220$  mbar and the integration step is  $\sim 0.2$  ns, which is approximately 1/3 of the mean collision time at that pressure.

The ion funnel model incorporates the solutions of the DSMC flow described with reference to Figure 2 in order to define the inlet boundary (capillary exit). The background pressure in the open boundary space described by the 10 mm gap between the capillary and entrance to ion funnel is set to 5 mbar. The boundaries at the outlet are determined by incorporating a second vacuum region separated by a 1.4 mm aperture from the funnel domain of the flow and set to  $10^{-2}$  mbar. The model was initiated with “no particles” and particle population increases progressively to satisfy the boundary conditions. The structure of the funnel is equivalent to the “breathless” low-capacitance geometry with 0.65 mm electrode thickness and 0.65 mm spacing. The i.d. of the first funnel electrode is 25.4 mm and the length of the system is 116 mm. The gap between the inlet boundary and the first funnel electrode is 10 mm.

Figures 4 (a) and (b) show solutions of the flow field for the axial and radial velocity components. The flow field shown does not represent a fully converged solution, but rather a snapshot of a calculation in progress. The current flow field is obtained after 6 weeks of calculations involving  $>40M$  particles traced with a 0.2 ns integration step on a single core machine. Some useful insights can be extracted for both the gas dynamical aspects of the flow and also the ion optical properties of the ion funnel despite the fact the calculation of the flow field is not yet complete.

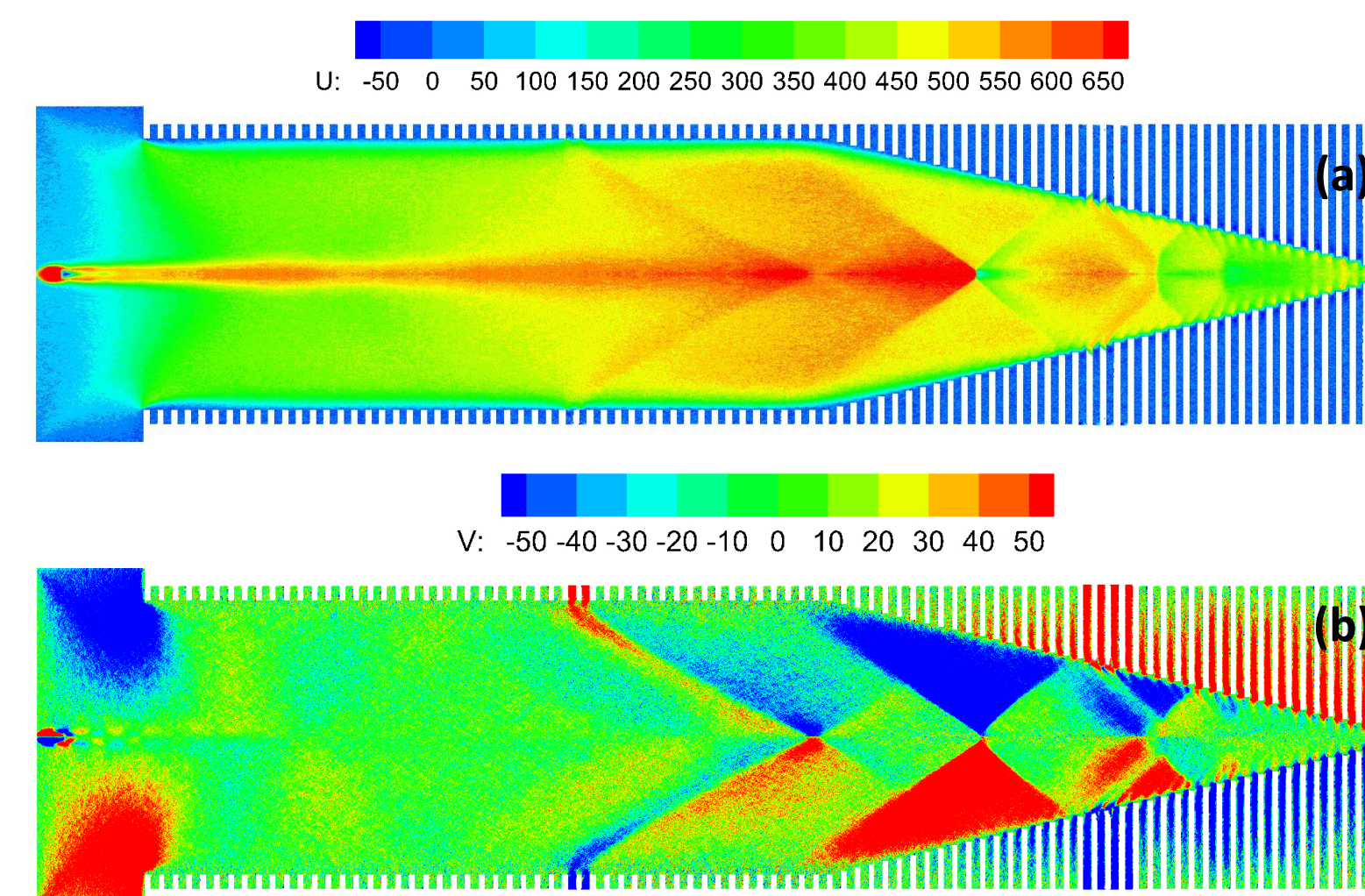


FIGURE 4. Flow fields for the (a) axial and (b) radial velocity components inside the ion funnel operated at 5 mbar pressure and discharging into a 10-2 mbar pressure region.

Figure 4 shows the formation of a narrow Mach disk followed by a diamond shock pattern in the near-field region of the jet, typical of the free jet expansion flow with a high jet pressure ratio. The near-field region appears to have no interaction with the ion funnel, in contrast to the far-field region where the jet penetration depth is affected by the electrode boundaries, as shown by a series of diagonal shocks formed and extending throughout the second half of the device. The velocity at the converging end exceeds 250 m/s and expected to have a significant contribution to the properties of the ion motion in the presence of RF and DC electric fields.

## ION OPTICS SIMULATIONS

The velocity flow fields shown in Figure 4 were post processed together with temperature and pressure and introduced in SIMION for tracing ions. The hard sphere collision model is employed to investigate the ion motion discussed with reference to the following Figures. Figure 5 (a) shows ion trajectories for  $m/z=133$  and (b) for  $m/z=1952$  corresponding to  $Cs^+$  and  $Cs_8I_7^+$  ions respectively. Ions are introduced into the flow from a 0.5 mm area appear to follow the structure of the flow with high precision. The high mass ions are radially deflected near the Mach disk and captured by the shear layer forming a ring, which is disrupted by the diagonal shocks established further downstream. The low mass ions are scattered via collisions early on forming a diffusive ion beam. Ion transmission as a function of RF settings applied to the funnel electrodes are shown in the following Figures 6 (a) and (b).

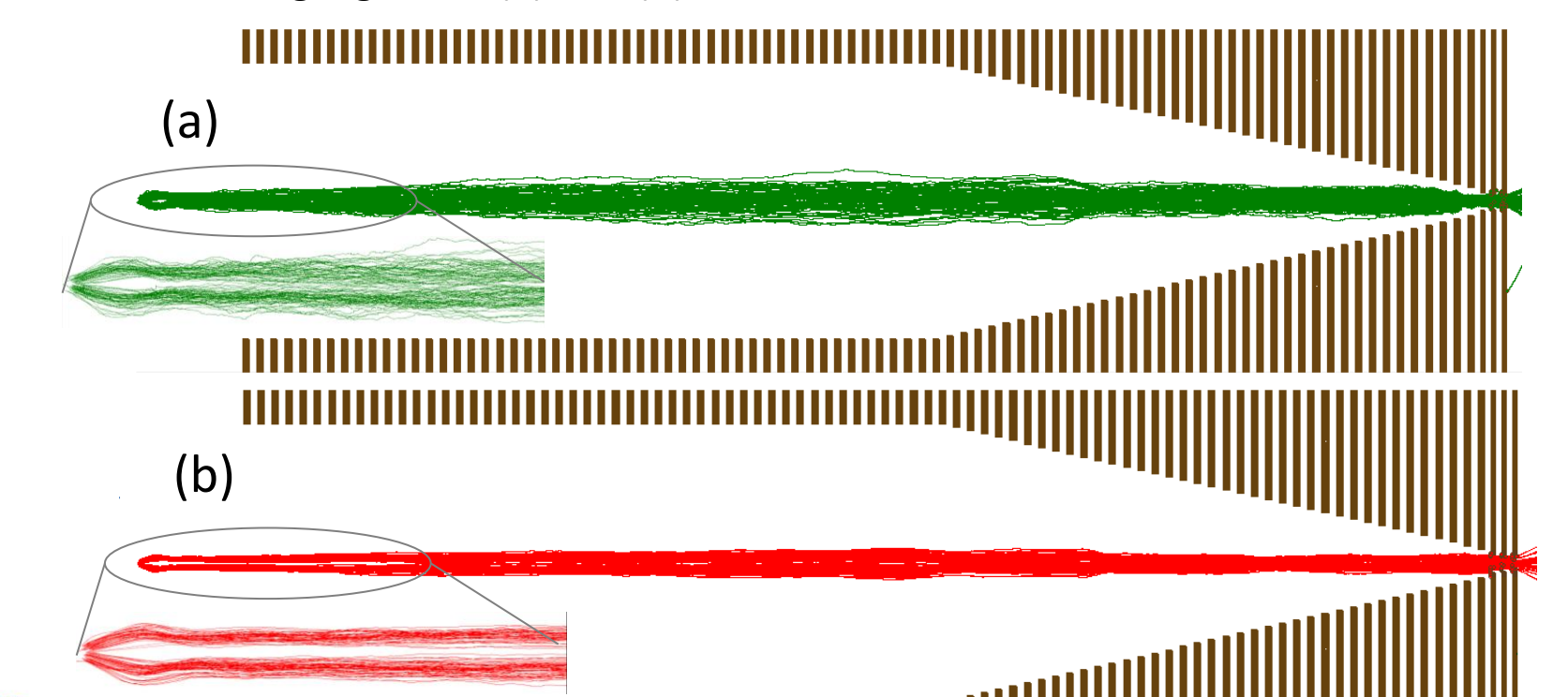


FIGURE 5. Ion trajectories inside the ion funnel in the presence of gas flow RF and DC field for (a)  $m/z=133$  and (b)  $m/z=1952$ .

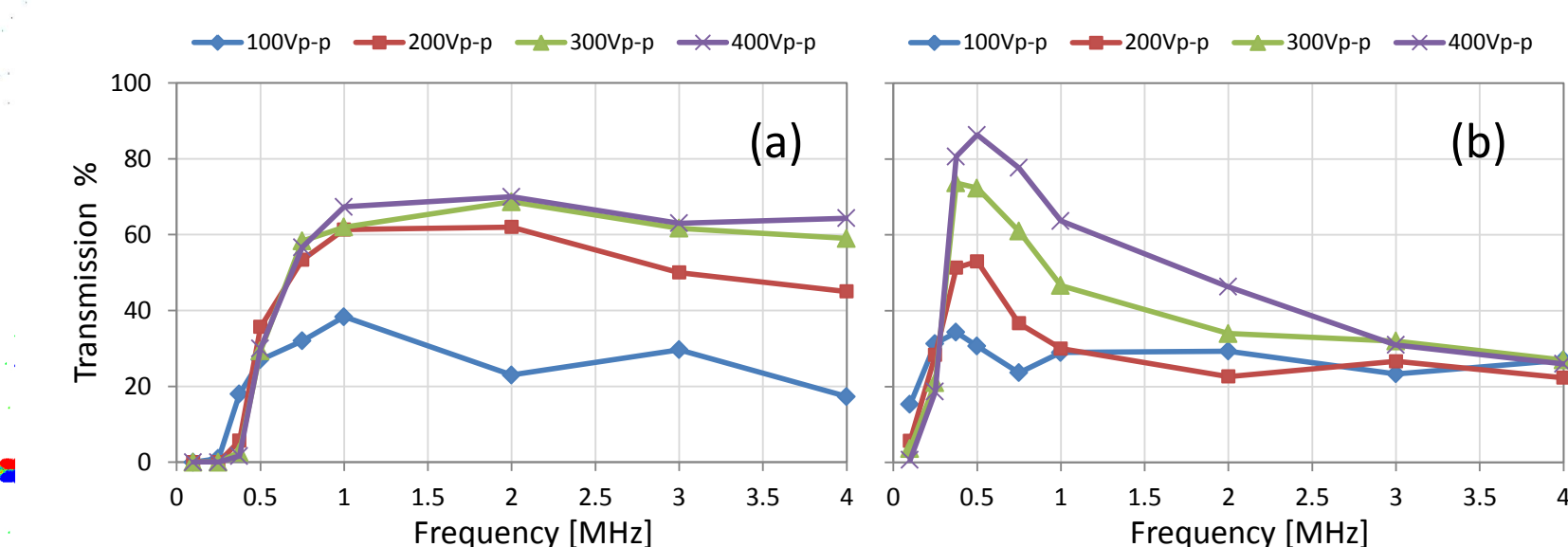


FIGURE 6. Ion transmission through the ion funnel in the presence of gas flow RF and DC fields for (a)  $m/z=133$  and (b)  $m/z=1952$ .

The DC voltage across the funnel in the simulation is set to 150 V. The last RF aperture is 2.5 mm and three consecutive DC electrodes are employed to reduce the size to 1.4 mm to maintain the necessary pressure difference. Figure 6 (a) shows ion transmission for  $m/z=133$  for different RF waveform amplitudes and for waveform frequencies extending from 0.2 to 4 MHz. Figure 6 (b) shows results for  $m/z=1952$ . In both cases transmission is enhanced for the highest RV voltage amplitude. The frequency for optimum ion transmission appears to be mass dependent. The high mass ion examined shows a distinct peak in transmission at 500 KHz and significantly lower transmission with increasing frequency. In contrast, the low mass ion reaches a maximum in transmission at 1 MHz without any significant drop as frequency is increased.

